Performance of Moving Target Parameter Estimation Using SAR

MATS I. PETTERSSON, Member, IEEE
THOMAS K. SJÖGREN, Member, IEEE
VIET T. VU, Member, IEEE
Blekinge Institute of Technology
Karlskrona, Sweden

Synthetic aperture radar (SAR) gives not only the opportunity to image targets with high resolution but also to measure their position and velocity. Without acceleration (constant speed), the position and velocity both in range and azimuth can be estimated using a multichannel SAR system. This paper introduces a method to find the lower bound on variance of estimate of position and velocity for targets. The method is based on the assumptions needed for the Cramér-Rao lower bound (CRLB). The method works for both narrowband (NB) and ultrawideband (UWB) SAR systems. For demonstration, a monostatic single-channel UWB SAR system operating at low frequency is used. Thus, only lower bounds for estimate variance of azimuth, range, and relative speed are derived.

I. INTRODUCTION

Ground moving target indication (GMTI) using a multichannel synthetic aperture radar (SAR) has been of interest to the scientific community for the last decades. It has been shown that a SAR system can detect moving targets and measure their properties [1–5]. The measurements not only give the information of a moving target but also the target surrounding such as e.g. houses and trees with very high accuracy. The performance of moving target estimation based on a dual-channel SAR system has been reported in [6] and the traditional solution of space time adaptive processing (STAP) with low resolution can be found in [7]. However, it has been shown that long integration time not only increases detectability but also adds the capability to measure radial speed and along-track components. This is of interest to all types of radar systems, especially to the lower frequency band SAR systems operating at, e.g. VHF/UHF bands. Parameter estimation for low-frequency systems is associated a with much longer integration time than at microwaves. In this case, small target accelerations do not destroy the coherence due to the long radar wavelength [8]. It can also be motivated like this: Let us assume that the maximum allowed phase error associated with an acceleration is limited to $\pi/8$. At 50 MHz this phase error is associated with a distance of approximately 40 cm and at 10 GHz is associated with a distance of 0.2 cm. This means that low frequencies are not sensitive to vibrations and smaller oscillations. This also means that the acceleration can occur for a much longer time at the low frequency without destroying coherency. The clutter density is also low in comparison with the system resolution. The clutter backscattering is therefore very stable between two measurements occasions, even if they are separated by days [9]. This means that statistical properties measured on one day can be used for the day after.

For the latest years, there has been a large interest in SAR processing of moving targets, demonstrated by the considerable number of publications of simulation and experimental results. In most publications, dual-channel and multichannel systems are taken into account. Besides this, single-channel systems are also used to detect and estimate moving target properties. Although the moving target detection and estimation methods are developed for narrowband (NB) systems, there are also theories determined for ultrawideband (UWB) [10–12] where the method in [10] is demonstrated in [8,13]. In NB SAR systems there have been many publications on moving target detection using only one antenna channel [3–5, 13–17]. The methods published in for example [14–17] use a single-channel NB SAR system to detect the target and estimate the target speed and acceleration. The basic idea is to use the phase of target range migration in combination with the antenna footprint. The illustration of the method is based on simulated and experimental data. However, detection based on dual-channel or multichannel systems is even more interesting due to the possibility to

suppress stationary targets, i.e., clutter. Estimating radial speed in dual-channel or multichannel SAR has been introduced in [18, 19]. In [20], the acceleration of the target is shown to be estimated using dual-channel SAR-GMTI and in [6], radial speed, relative speed, and acceleration are determined. That means that all speed components can be determined if flat Earth and no acceleration are assumed.

Let us have a look at estimation precision. A method to estimate measurement precision in a SAR-GMTI system can be characterized in two different ways, not considering clutter and noise and considering it. The first way is probably the most common one and based on the resolution concept that the measurement precision is limited by the resolution. As shown in [21], the resolution in relative speed is proportional to the inverse of the synthetic aperture square of the length, a result that also can be found in [22] where the step size in detection is based on the resolution in relative speed. In [21], the resolution of range and azimuth position and the resolution in relative speed can be retrieved. In this case the clutter and noise and the coupling between range and azimuth have not been considered. If clutter and noise is considered, all publications are limited to NB systems. In [23], the Cramér Rao lower bound (CRLB) of a moving target position at minimum range is derived and the main interest is the radial speed component. In [24, 25], the radial speed estimation precision is introduced for an along-track interferometric SAR system. The derivations in [24] also consider the bound for two different models of the moving target response, i.e., deterministic and zero-mean Gaussian. The lower bound takes target strength, clutter, and noise into account. In [25], the CRLB for radial speed is calculated.

In this paper, we derive a method to calculate CRLB for single-channel or multichannel UWB SAR systems. The derivation is based on a point-like scattering moving target. The CRLB is found for scattering amplitude, scattering phase, range position, azimuth position, and velocity. Depending on the number of channels of the considered SAR system, i.e., single channel or multichannel, the relative speed or the range and azimuth speed CRLB is determined. In the published papers mentioned above, backscattering amplitude, phase, and radial speed CRLB are mainly aimed at, whereas in this paper we derive a method that can provide up to six parameters of CRLB, depending on the number of channels of the SAR system. The method presented, in comparison with the previous publications, is not restricted by NB systems. The idea of the method was first mentioned in [26]. For simplification in the presentation, we consider the correlation for an intermediate bandwidth (frequency bandwidth approximately center frequency and integration angle less than 32 deg) SAR image instead of multichannel UWB SAR images. The illustration of the method is therefore based on a single-channel SAR system. One reason for this choice is that we do not have a good model of the correlation matrix for a multichannel

UWB SAR system. The other is that there are single-channel data results to compare with in [8, 13] and the results given in [21].

The paper is organized as follows. The moving target's parameter vector and motion model are presented in Section II. The signal model, which is used to develop the method, is given in Section III. The measurement signal is given in Section IV and the clutter and noise model is discussed and motivated in Section V. In Section VI, the measured signal model is motivated. Section VII aims at SAR image sampling and correlation between the image samples. The CRLB of moving target parameters are derived in Section VIII. Section IX provides numerical calculation of lower bounds in position and relative speed. Conclusions are presented in Section X.

II. MOVING TARGET'S PARAMETER VECTOR AND MOTION MODEL

When a target is moving on the Earth's surface, its motion can be described in a local Cartesian coordinate system by $(\xi_T(t), \eta_T(t), \zeta_T(t))$. Since the Earth is approximately flat, the target location is simplified to $(\xi_T(t), \eta_T(t), 0)$. Detection of low signature targets or detection in low-frequency SAR is associated with a large integration angle and in most cases therefore also with a long integration time. Detection of very slow moving targets is also associated with a long integration time, i.e., measurement time needed to discriminate Doppler from slow target to the surrounding clutter. At low frequencies, the signal wavelengths are long and therefore not very sensitive to target vibration and acceleration. Thus, a fairly good approximation, at least at low frequencies, for a moving target is to assume that there is neither vibration nor acceleration. The target position in Cartesian coordinates is expressed by

$$
\begin{aligned}
&(\xi_T(t), \eta_T(t), \zeta_T(t)) \\
&= (\xi_0 + v_\xi(t - t_0), \eta_0 + v_\eta(t - t_0), 0)
\end{aligned} \quad (1)
$$

where ξ_0 and η_0 are the ground positions at time of the minimum range t_0, and v_ξ and v_η are the constant speed components. The platform motion is often described in a similar way as

$$
(\xi_{pl}(t), \eta_{pl}(t), \zeta_{pl}(t)) = (v_{pl}t, 0, h) \quad (2)
$$

where v_{pl} denotes the speed and h is the altitude over ground of the platform. If more antennas are used, the true position of each antenna channel needs to be considered, especially in the case of UWB [27]. Let us consider a point-like scatterer with the backscattering strength S_T and phase ϕ_T. The target parameters are represented by a vector as

$$
\boldsymbol{\theta} = \begin{bmatrix} \xi_0 & \eta_0 & v_\xi & v_\eta & S_T & \phi_T \end{bmatrix} \quad (3)
$$

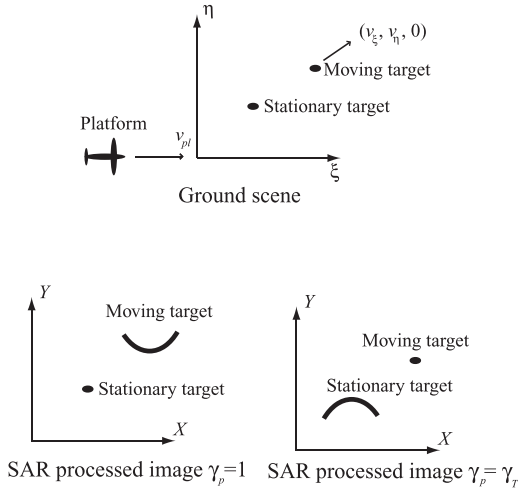Since the SAR image formation is seen as a linear process, the moving target parameter vector can be found from the

Fig. 1. Illustration of ground scene and corresponding SAR images processed at different relative speeds.

image reconstructed by the l-channel SAR data [10],

$$\boldsymbol{\theta} = [X_0 \ Y_0 \ \Delta X_{0l} \ \Delta Y_{0l} \ S_T \ \phi_T] \quad (4)$$

where X_0 and Y_0 are the azimuth and range positions at t_0 of the moving target on the SAR image formed by the first channel data and ΔX_{0l} and ΔY_{0l} indicate the displacements between the images reconstructed from the first channel and the l-th channel data. The relationship between displacement and location can be found, e.g. in [10]. Depending on the focusing parameter, i.e., the processed relative speed, a moving target is either focused, when the processed relative speed is the same as the true relative speed of the target, or smeared as a curve, when an incorrect relative speed is used for processing, Fig. 1. This may result in a large reduction in the target resolution and the target peak energy level [22]. The mathematical description of the moving targets smeared as a curvature is presented, e.g. in [28] and this smeared effect is clearly shown by the experimental data in [8].

In this paper, we propose a method to estimate the lower bound for target parameter estimation variance. The theory is presented in the next sections and based on a measurement vector given by stacking all channels and all SAR image samples. In the illustration of the proposal, we use only one channel data, i.e., only one SAR image. In this case only the focusing can be applied resulting in a relative speed estimate leaving the full movement and displacement in azimuth unresolved. This makes the illustration simpler with only five parameters to estimate instead of six in case of a multichannel SAR system. The lower bound is therefore independent of channel separation, a parameter that is very system dependent. The selection of one channel data is also for comparison purpose. Thus, the lower bound can be related to the relative speed estimates in [8, 13] and the result presented in [21]. Hence, the parameters that can be estimated in one channel data are given by

$$\boldsymbol{\theta} = [X_0 \ Y_0 \ \gamma_T \ S_T \ \phi_T] \quad (5)$$

where γ_T is the normalised version of the relative speed or the normalised relative speed (NRS) and given by

$$\gamma_T = \sqrt{(v_{pl} - v_\xi)^2 + v_\eta^2} \Big/ v_{pl} \quad (6)$$

The fundamental principal in SAR processing is to handle range migration. The distance between the moving target and the platform is given by

$$r_T(t) = \sqrt{(\xi_{pl}(t) - \xi_T(t))^2 + (\eta_{pl}(t) - \eta_T(t))^2 + \zeta_{pl}^2(t)} \quad (7)$$

Assuming no acceleration as in (1) the distance refers to

$$r_T(t) = \sqrt{\gamma_T^2(\xi_{pl}(t) - X_0)^2 + Y_0^2} \quad (8)$$

in image coordinates where derivations can be found in for example [10]. The one channel SAR image position (X_0, Y_0) and the true position (ξ_0, η_0) are unresolved due to the displacement in azimuth caused by range speed [29] (NB SAR) or by NRS (range and azimuth speed components UWB SAR) [10]. Similarly, the distance from the platform to any image sample (X, Y) in the SAR image processed at a relative speed γ_p is shown to be [22]

$$r_p(t, X, Y, \gamma_p) = \sqrt{\gamma_p^2(\xi_{pl}(t) - X)^2 + Y^2} \quad (9)$$

where γ_p is the processed NRS.

III. MOVING TARGET SIGNAL MODEL

To determine the lower bound of the variance for a parameter estimate, it is necessary to build an appropriate model of the signal, clutter, and noise. Under a point-like scattering approximation and a nonacceleration assumption, one channel SAR image (reconstructed with no clutter and noise) is represented by the integral

$$h_s(X, Y, \gamma_p, \boldsymbol{\theta}) = \int_{T_1}^{T_2} g\left(t_s, \frac{2r_p(t_s, X, Y, \gamma_p)}{c_0}, \boldsymbol{\theta}\right) dt_s \quad (10)$$

where $g(t_s, t_f, \boldsymbol{\theta})$ is the pulse-compressed impulse response of a point moving target in fast time t_f and in slow t_s, T_1 is the start of the measurements, and T_2 is stop of the measurement in slow time. Equation (10) is therefore used as the signal of the target in parameter estimation. Measurement time is often considered to be infinite in SAR processing. Conversely, a finite measurement time is set by the impulse response of $g(t_s, t_f, \boldsymbol{\theta})$ in t_s and in t_f. The impulse response depends on system parameters such as selected waveform, antenna gain function, range distance, and target scattering characteristics. In this paper, we use a simple model with a transmitted chirp pulse, flat receiver characteristics, an isotropic antenna element, no acceleration on target and platform, point-like scattering characteristics for stationary scatterers (clutter), and the moving target. For L-channels, a vector is formed by stacking $L \times N \times M$ image samples

together where N is the number of range positions and M is the number of azimuth positions. As discussed above we illustrate the method for one channel, and in this case the stacking results in a steering vector given by

$$
\begin{aligned}
\tilde{\boldsymbol{\mu}}_s \left(\gamma_p, \boldsymbol{\theta} \right) \\
= \big[h_s \left(1, 1, \gamma_p, \boldsymbol{\theta} \right) \quad \cdots \quad h_s \left(1, M, \gamma_p, \boldsymbol{\theta} \right) \\
h_s \left(2, 1, \gamma_p, \boldsymbol{\theta} \right) \quad \cdots \quad h_s \left(N, M, \gamma_p, \boldsymbol{\theta} \right) \big]^T
\end{aligned} \tag{11}
$$

With K transmitted pulses along the synthetic aperture, the steering vector components are given by

$$
\begin{aligned}
\tilde{\mu}_s \left(m_s \left(n, m \right), \gamma_p, \boldsymbol{\theta} \right) = h_s \left(n, m, \gamma_p, \boldsymbol{\theta} \right) = \\
= \sum_{k=1}^{K} g \left(t_s \left(k \right), \frac{r_p \left(k, n, m, \gamma_p \right)}{c_0}, \boldsymbol{\theta} \right)
\end{aligned} \tag{12}
$$

where $m_s \left(n, m \right)$ is the stacked index given by n and m, and $r_p \left(k, n, m, \gamma_p \right) = r_p \left(t_s \left(k \right), X \left(n \right), Y \left(m \right), \gamma_p \right)$ is the discrete distance for pulse k to image pixel $\left(X \left(n \right), Y \left(m \right) \right)$.

IV. MEASUREMENT SIGNAL

The measured samples will not only contain a signal from the moving target $\tilde{\mu}_s \left(m_s \left(n, m \right), \gamma_p, \boldsymbol{\theta} \right)$ but also backscattering from clutter and noise. An image sample is given by a superposition of the pulses along the synthetic aperture and can therefore be rewritten to a sum of measurements as

$$
\begin{aligned}
\tilde{\mu}_{\tilde{x}} \left(m_s \left(n, m \right), \gamma_p, \boldsymbol{\theta} \right) = h_{\tilde{x}} \left(n, m, \gamma_p, \boldsymbol{\theta} \right) \\
= \sum_{k=1}^{K} p_{\tilde{x}} \left(k, \frac{r_p \left(k, n, m, \gamma_p \right)}{c_0}, \boldsymbol{\theta} \right)
\end{aligned} \tag{13}
$$

where $h_{\tilde{x}} \left(n, m, \gamma_p, \boldsymbol{\theta} \right)$ is the sampled SAR image processed at relative speed γ_p, $p_{\tilde{x}} \left(k, t_f, \boldsymbol{\theta} \right)$ is the pulse-compressed received signal at aperture position k that contains the backscattering from the moving target and the clutter and also the noise. The pulse repetition interval (PRI) or pulse repetition frequency (PRF) is a design parameter that will affect the correlation between samples.

V. CLUTTER AND NOISE MODEL

The precision in the estimation of the moving target's parameter vector depends on clutter and noise. For radar systems, the signal interference is commonly divided into two independent groups: clutter generated by scatterers in the illuminated area and noise originated from thermal processes in the receiver or high equivalent antenna temperatures. In this study, we concentrate on the lower bound of variance for parameter estimation and therefore the covariance between SAR image samples. In the stacked measurement vector $\tilde{\boldsymbol{\mu}}_{\tilde{x}} \left(\gamma_p, \boldsymbol{\theta} \right)$, the correlation between image samples is defined by

$$
\mathbf{C}_{\tilde{x}} \left(\gamma_p, \boldsymbol{\theta} \right) = E \left[\boldsymbol{\mu}_{\tilde{x}} \left(\gamma_p, \boldsymbol{\theta} \right) \boldsymbol{\mu}_{\tilde{x}}^H \left(\gamma_p, \boldsymbol{\theta} \right) \right] \tag{14}
$$

Let us first in the derivation of the clutter and noise model assume that the target influence on the clutter and noise is so weak that the target can be neglected and that the statistics are zero mean. Because the clutter and noise are independent [10], the correlation can be found from

$$
\mathbf{C}_{\tilde{x}} \left(\gamma_p, \boldsymbol{\theta} \right) = \mathbf{C}_{\mathbf{c}} \left(\gamma_p, \boldsymbol{\theta} \right) + \mathbf{C}_{\mathbf{n}} \left(\gamma_p, \boldsymbol{\theta} \right) \tag{15}
$$

Starting with the noise statistics, neglecting target and clutter, the measured noise sample would be

$$
\tilde{\mu}_n \left(m_s \left(n, m \right), \gamma_p, \boldsymbol{\theta} \right) = \sum_{k=1}^{K} p_n \left(k, \frac{r_p \left(k, n, m, \gamma_p \right)}{c_0}, \boldsymbol{\theta} \right) \tag{16}
$$

where $p_n \left(k, t_f, \boldsymbol{\theta} \right)$ is measured pulse-compressed noise. A common model for the noise is that it consists of white Gaussian noise with zero mean at the antenna. The measured $p_n \left(k, t_f, \boldsymbol{\theta} \right)$ will be colored and set by the bandwidth of the receiver and the antenna. For high equivalent antenna temperature, as for example low-frequency radar, the antenna is important, while at many microwave bands equivalent antenna temperature is low and the noise is set by the receiver noise. Therefore, the correlation of $p_n \left(k, t_f, \boldsymbol{\theta} \right)$ in range will be limited by the bandwidth of the noise and in azimuth by the PRF of the system. The spectrum of noise is assumed to be flat in the frequency domain. The correlation of $p_n \left(k, t_f, \boldsymbol{\theta} \right)$ is therefore set by the system impulse response, which is a sinc function in azimuth and in range in the raw data. Hence, the correlation of $\tilde{\boldsymbol{\mu}}_n \left(\gamma_p, \boldsymbol{\theta} \right)$ will be given by the impulse function set by the receiver bandwidth, the PRF of the system, and the Doppler filtering performed in the SAR processing. The SAR processing forms a noise spectrum similar to that formed by the clutter.

For the clutter excluding the noise and the target, the correlation $\mathbf{C}_{\mathbf{c}} \left(\gamma_p, \boldsymbol{\theta} \right)$ is given by the statistical properties of

$$
\tilde{\mu}_c \left(m_s \left(n, m \right), \gamma_p, \boldsymbol{\theta} \right) = \sum_{k=1}^{K} p_c \left(k, \frac{r_p \left(k, n, m, \gamma_p \right)}{c_0}, \boldsymbol{\theta} \right) \tag{17}
$$

where $p_c \left(k, t_f, \boldsymbol{\theta} \right)$ is the measured pulse-compressed clutter signal. In comparison with $p_n \left(k, t_f, \boldsymbol{\theta} \right)$, $p_c \left(k, t_f, \boldsymbol{\theta} \right)$ will be limited in Doppler by the wavelength and the speed of the platform. $p_c \left(k, t_f, \boldsymbol{\theta} \right)$ will be correlated between pulses at distance $r_p \left(k, n, m, \gamma_p \right)$ with $\gamma_p = 1$. For one clutter scatterer on the ground, the backscattering has a very strong correlation between k-th samples along the synthetic aperture. Traditionally, the SAR resolution cells are assumed to include a large number of scatterers, which results in speckle processes between the scatterers inside the resolution cell. The most commonly used models assume large number of scatterers that from the central limit theorem cause the real and imaginary backscattering part to be normally distributed. However the number of scatterers in a resolution cell in a UWB system will decrease dramatically and the
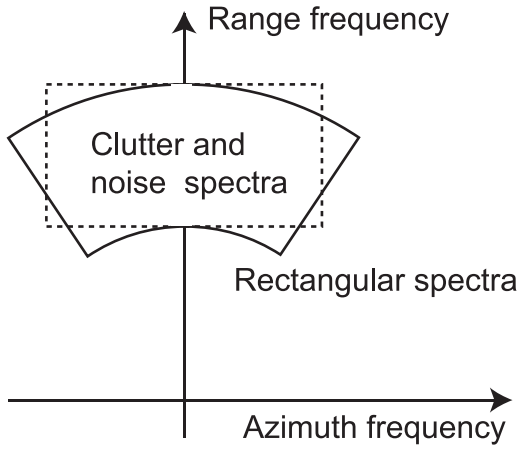
Fig. 2. Clutter and noise spectra in UWB SAR image (——) in comparison with NB assumption of rectangular SAR image spectra (---).

traditional clutter model will not be valid in many cases. Especially at low frequency the number of scatterers in the resolution cell will come close to one when the resolution gets smaller than the operating wavelength. It is only in heavily forested areas that the number of scatterers could be more than one (if volume scattering occurs), while in open areas the number of scatterers per resolution cell will often be much less than one. For UWB low-frequency systems used over open areas the number of scatterers may be extremely low and the backscattering straight so low that the weak scatterers could be hidden in the noise. In these cases there is no model available for UWB SAR clutter modelling. However, in this paper we assume that the backscattered area is homogenous and that each clutter scatterer could be assumed to be normally distributed in its real and imaginary parts. This is a common scatter model and can for example be found in [30].

In radar backscattering models, the radar backscattering appears from a homogenous area with a large number of scatterers. For one pulse along the synthetic aperture the resolution area is given by the area of a circular annulus on the ground limited by the impulse bandwidth of $p_{\tilde{x}}(k, r_p(k, n, m, \gamma_p)/c_0, \theta)$ and the antenna footprint. The resolution in a UWB SAR system is for one pulse very low due to the wide antenna footprint. Adding two pulses together $p_{\tilde{x}}(k, r_p(k+1, n, m, \gamma_p)/c_0, \theta) + p_{\tilde{x}}(k, r_p(k, n, m, \gamma_p)/c_0, \theta)$ with the proper range will make a large overlap between the pulses causing many clutter scatterers to correlate between pulses. As the number K of pulses increases in (13), resolution increases in the processed SAR image if a proper range compensation is made, depending, however on the possibilities to perform range compensation. If the focusing parameter is set to a moving target, i.e., $\gamma_p = \gamma_T \neq 1$, the resolution for clutter decreases in comparison with the case $\gamma_p = 1$ and therefore the number of clutter scatterers increases in the SAR image resolution cell. The lower resolution of the clutter will cause a larger correlation between pixels in the SAR image, because the

sampling criteria of the SAR image are set by moving targets that are focused. We therefore conclude that change of the processing speed will affect the correlation $\mathbf{C}_{\tilde{x}}(\gamma_p, \theta)$ between pixels in the SAR image.

In range direction the SAR raw data spectra of the clutter are set by the bandwidth of the transmitted and received pulse. This is the same limitation as for the noise if the received signal has the same band limitation as the transmitted signal. In the azimuth direction of the SAR raw data spectra, the clutter however behaves differently compared with the noise as described above. However after backprojection both clutter and noise are on an annulus segment. The conclusion is that the spectrum of the clutter and noise is approximately a square when the SAR system is an NB system, but not when it is a UWB system, Fig. 2. The clutter correlation $\mathbf{C_c}(\gamma_p, \theta)$ can be found from the SAR image impulse response. The impulse response for an NB system is a sinc function while it is much more complicated for a UWB system [31]. The method presented in the paper is able to handle even the complicated statistics given by the UWB SAR image clutter. However in the selected example there are limitations in bandwidth and in integration angle as mentioned in Section II.

VI. MEASURED SIGNAL MODEL

In this paper we do not exclude long integration time in the estimation phase, and therefore the algorithm has to handle the nonlinear range migration over the aperture. In the SAR image plane the stationary clutter will be unfocused as γ_p separates from one, and the dependency between the elements in the covariance matrix increases. The noise is independent of the clutter and the target. The question is the dependence between clutter and target. Electromagnetic scattering is superimposed from different scatterers. If scattering of each scatterer does not interact with another scatterer, they can be considered to be independent. This will be justified if the Born approximation [32] holds for both the clutter and the target scatterers. However, in many cases there are multipath backscattering and shadowing effects in the backscattering process. Despite that, the Born approximation is a good model in a resolution cell with many scatterers and therefore

$$\tilde{\mu}_{\tilde{x}}(\gamma_p, \theta) = \tilde{\mu}_s(\gamma_p, \theta) + \tilde{\mu}_c(\gamma_p) + \tilde{\mu}_n(\gamma_p) \quad (18)$$

is often used. Note that if clutter and noise are independent of the target they are also independent of target parameter vector θ, and therefore the clutter and noise only depends on the focusing parameter. For UWB SAR, this approximation may be more questionable as the resolution of a UWB SAR system is about the same size as a scatterer. Backscattered clutter in the neighbouring resolution cell to the target will therefore be influenced by that target through multipath scattering or by shadowing effects. For a moving target the scattering process will be even more complicated. If the integration time is long, the

target will pass many clutter scatterers during illumination. Many clutter scatterers will therefore multiscatter with the moving target or be shadowed by the target for a short period of time as the target passes. To our knowledge, these effects have not been investigated in any publication. We therefore use independency as the best available model. However, in the later simulations, the approximation is correct. For real data, we believe that the error caused by the approximation is rather small and therefore conclude that the measured signal model is given by (18). We have then made use of the circumstance that the SAR process is a linear system that will not change the independency.

VII. SAR IMAGE SAMPLING AND CORRELATION BETWEEN THE SAMPLES

To estimate the target speed a focusing approach can be applied to the target [4]. For all SAR systems moving targets are focused when the correct NRS is used in the SAR process. However NB systems are mainly sensitive to azimuth speed because even small changes in v_ξ changes NRS much more than small changes of v_η. For long integration time as associated with a UWB SAR system to produce a focused SAR image of a moving target, the correct NRS has to be considered $\gamma_p = \gamma_T$. The target is then focused whereas the clutter gets unfocused and smeared. If the clutter speed is used for focusing $\gamma_p = 1$, the moving target will be smeared to either an elliptic or a hyperbolic function [33]. The smearing effect of a moving target is clearly illustrated both in simulation and on real data in [8]. In [28] the curve, i.e., the image coordinates $\left(X_p^T, Y_p^T\right)$ along which the target energy smears are given by

$$\frac{\left(Y_p^T\right)^2}{Y_0^2} + \frac{\gamma_p^2 \gamma_T^2}{\gamma_T^2 - \gamma_p^2} \frac{\left(X_0 - X_p^T\right)^2}{Y_0^2} = 1 \qquad (19)$$

Equation (19) is the equation of an ellipse if $\gamma_p < \gamma_T$ and a hyperbolic function if $\gamma_p > \gamma_T$. On one hand, the trajectory in (19) illustrates a decrease in resolution as the incorrect speed is used in processing which can be used for the clutter. On the other hand, it also illustrates an increase in correlation between image samples as the clutter gets unfocused. There are two natural choices: generating a focused image of a moving target or generating an image of focused stationary targets such as clutter. In this paper we select the clutter speed, i.e., $\gamma_p = 1$. The reason is that the energy of the clutter is more focused and therefore the SAR image samples are less correlated.

To calculate the lower bound, the correlation matrix of the measurement vector $\tilde{\mu}_{\tilde{x}}\left(\gamma_p, \theta\right)$ is needed, i.e., the correlation between image samples and between antenna channels. With one channel SAR, as illustrated in Section IX, only the correlation between image samples is needed to find $C_{\tilde{x}}\left(\gamma_p, \theta\right)$. The correlation is given by the correlation between clutter scatterers and influenced by the system impulse response. In NB SAR, it is common to use independency between image samples. The

independency between samples is often formed by sampling data on the Nyquist limit [34]. This can easily be made in an image that is processed from white noise and system impulse response of a sinc function. For a SAR image it is, however, different. As mentioned before, the clutter and noise spectrum is approximately a pie-shaped region and therefore the sinc function approximation will fail. At NB, however, the spectrum is approximately a rectangular region and the approximation can be used. The question is therefore at how big integration angles and at how big bandwidth can the approximation of independent samples can be used? This is adequately illustrated in [31] where three spectra are shown with different integration angles and different bandwidths. The frequency bandwidth is often characterized in relative bandwidth

$$B_r = \frac{f_{\max} - f_{\min}}{f_c} \qquad (20)$$

where $f_{\max}, f_{\min}$, and f_c are the system maximum, minimum, and centre frequency, respectively. For the intermediate SAR system, the relative bandwidth B_r of 0.35 and an integration angle ϕ_0 of 35 deg gives a close to sinc-like impulse response with orthogonal sidelobes in range and azimuth direction. However, this rather wideband system tends to have nonorthogonal sidelobes that will, for higher bandwidths, break up to nonorthogonal sidelobes that are not sinc-like [31, 35]. Due to the nonorthogonal structure and the non-sinc-like shape, the correlation will increase between the samples even if the sampling is chosen in a way considered optimum in NB SAR. The nonorthogonality and the non-sinc-like shape are caused by the coupling of range and azimuth. The increased effect of coupling as the bandwidth in azimuth and range increases is shown in [35]. In that paper, broadening factors in range and azimuth are derived that relate the real impulse response to a sinc function. It therefore gives a good indication of in which ranges of bandwidths and integration angles the NB approximation will be appropriate for the correlation. The article also shows that if the resolution is the same in azimuth and range, the NB approximation holds for larger bandwidths. This means that as the resolution increases the range and azimuth should increase in both directions, for a low correlation. The highest broadening factors, and therefore presumably the highest correlation, are given at low range resolution and high azimuth resolution. A low correlation between image samples is found (at Nyquist) if corresponding broadening factors are close to one. As we have not determined the UWB correlation in this study, we limit the evaluation to the area where $B_r \leq 1$ and $\phi_0 \leq 32°$. By evaluating the impulse response of the simulated systems, we found that pixels have low correlation in this interval using Nyquist limits. However, the highest correlation occurs when B_r mismatches ϕ_0 (in resolution) and in particular when the range resolution is low and the azimuth resolution is high.

In the evaluation Section IX we use $B_r \leq 1$, $\phi_0 \leq 32°$, $\gamma_p = 1$, and the image sampling proposed in this section.

According to the motivation above, the vector elements in $\tilde{\boldsymbol{\mu}}_c\left(\gamma_p, \boldsymbol{\theta}\right)$ are independent. This results in that the $\mathbf{C_c}\left(\gamma_p\right)$ is a diagonal matrix. The assumption diagonal covariance is only valid for single-channel SAR systems.

VIII. CRAMÉR RAO LOWER BOUND OF MOVING TARGET PARAMETERS

Under the assumption that the clutter backscatter and the thermal noise are complex normally distributed at the antenna input, and the SAR image formation is a linear process, the image samples are also complex normally distributed. With this statement, the estimation performance can be evaluated from the well-known CRLB. In its complex form, the lower bound of the variance for the parameter estimate is found to be [34]

$$\mathbf{C}_{\hat{\boldsymbol{\theta}}} \geq \mathbf{I}^{-1}\left(\boldsymbol{\theta}\right) \qquad (21)$$

where each element in the Fischer information matrix is

$$I_{ij}(\boldsymbol{\theta}) = tr\left[\mathbf{C}_{\tilde{x}}^{-1}\left(\gamma_p, \boldsymbol{\theta}\right)\frac{\partial \mathbf{C}_{\tilde{x}}\left(\gamma_p, \boldsymbol{\theta}\right)}{\partial \theta_i}\mathbf{C}_{\tilde{x}}^{-1}\left(\gamma_p, \boldsymbol{\theta}\right)\frac{\partial \mathbf{C}_{\tilde{x}}\left(\gamma_p, \boldsymbol{\theta}\right)}{\partial \theta_j}\right]$$
$$+ 2\mathrm{Re}\left[\frac{\partial \tilde{\boldsymbol{\mu}}_s^H\left(\gamma_p, \boldsymbol{\theta}\right)}{\partial \theta_i}\mathbf{C}_{\tilde{x}}^{-1}\left(\gamma_p, \boldsymbol{\theta}\right)\frac{\partial \tilde{\boldsymbol{\mu}}_s\left(\gamma_p, \boldsymbol{\theta}\right)}{\partial \theta_j}\right]$$
$$(22)$$

In this study, we assume that the clutter backscattering is independent on the target motion as discussed in the previous sections. With the knowledge of noise that is independent of target and clutter, the Fisher information is reduced to

$$I_{ij}\left(\boldsymbol{\theta}\right) = 2\mathrm{Re}\left[\frac{\partial \tilde{\boldsymbol{\mu}}_s^H\left(\gamma_p, \boldsymbol{\theta}\right)}{\partial \theta_i}\mathbf{C}_{\tilde{x}}^{-1}\left(\gamma_p\right)\frac{\partial \tilde{\boldsymbol{\mu}}_s\left(\gamma_p, \boldsymbol{\theta}\right)}{\partial \theta_j}\right] \qquad (23)$$

where the target, clutter, and noise independency cause the first part of (22) to be zero, i.e.,

$$tr\left[\mathbf{C}_{\tilde{x}}^{-1}\left(\gamma_p, \boldsymbol{\theta}\right)\frac{\partial \mathbf{C}_{\tilde{x}}\left(\gamma_p, \boldsymbol{\theta}\right)}{\partial \theta_i}\mathbf{C}_{\tilde{x}}^{-1}\left(\gamma_p, \boldsymbol{\theta}\right)\frac{\partial \mathbf{C}_{\tilde{x}}\left(\gamma_p, \boldsymbol{\theta}\right)}{\partial \theta_j}\right] = 0$$
$$(24)$$

This is a consequence of the Born approximation discussed in Section V and by this the assumed independency between target and clutter scatterer is valid in (18). It is also consistent with lower bound estimates based on STAP [7].

IX. ILLUSTRATION OF THE PROPOSED METHOD BY NUMERICAL CALCULATION OF LOWER BOUNDS IN POSITION AND RELATIVE SPEED

To illustrate the method, we estimate the lower bound for a simple case with a simulated moving point-like scatterer (target), and the clutter and noise statistics determined in Section VII. As mentioned, the measurement vector is formed by stacking the image samples together in a long vector given in (13). The illustration of the proposed method uses single-channel data. However, this should not be seen as a limitation and

the method can as discussed preferably be used on multichannel data (4). The extension is only to stack the antenna channels in the measurement vector. The estimation results are very dependent on radar system parameters. In this illustration, we select radar system parameters related to published results in [8,13]. These typical cases are selected due to the very long integration time associated with the experiments ($>$30 s). For many moving targets a very long integration time cannot be used without considering acceleration. However the long integration time and the UWB SAR case should not be seen as a restriction of the method and it works well also for short integration time and the NB case.

In CLRB, the covariance and derivation of the steering vector are needed. The clutter covariance $\mathbf{C_c}\left(\gamma_p, \boldsymbol{\theta}\right)$ is found using the assumption of independent samples described in Section VII, which relates to the clutter correlation and is set by the impulse response in the SAR image. As mentioned earlier, the correlation length is affected by the separation between the processed NRS and the NRS of the imaged target. The clutter correlation between SAR image pixels increases as γ_p separates from 1 as discussed in Section VII and illustrated in Fig. 1. The correlation is therefore minimum at $\gamma_p = 1$ for stationary scatterers, i.e., clutter. To use independency between pixels in the SAR image, $\gamma_p = 1$ is selected for the processing. The PRF is in the simulation set to be equal to Nyquist of the maximum clutter Doppler (the target speed is assumed to be much less than the platform speed and the antenna footprint is assumed to be isotropic). Doppler is always limited by operating wavelength, platform speed, and antenna footprint. The selected PRF also sets the limit for the noise described in Section V. Solving (21) and (23) numerically gives us the uncertainty of the parameter vector given in (4) or (5). Because we use one channel in this illustration we estimate the accuracy of five parameters given by the diagonal elements of the inverted Fisher information. The three interesting parameters lower bound of estimate variance is

$$\sigma_{\hat{X}_0}^2 = \left(\mathbf{I}^{-1}\left(\boldsymbol{\theta}\right)\right)_{11}$$
$$\sigma_{\hat{Y}_0}^2 = \left(\mathbf{I}^{-1}\left(\boldsymbol{\theta}\right)\right)_{22}$$
$$\sigma_{\hat{\gamma}_t}^2 = \left(\mathbf{I}^{-1}\left(\boldsymbol{\theta}\right)\right)_{33} \qquad (25)$$

where $\sigma_{\hat{X}_0}^2$ is the lower bound for the target position in azimuth, $\sigma_{\hat{Y}_0}^2$ is the lower bound for target position in range, and $\sigma_{\hat{\gamma}_t}^2$ is the lower bound for target relative speed.

For this example, the main steps in obtaining the bounds for variance of the parameter estimates are described in algorithm 1. The SAR image is made according to Section VII. By this, a diagonal covariance matrix can be used under the made beamwidth and bandwidth restrictions. The function to generate the SAR image in algorithm 1 selects the size of the SAR image. This is done by considering the extension of the smeared moving target and that is found using (19). For different integration angles, the size of the SAR image will change

due to SAR sampling and the smearing effect of the target. In this illustration the SAR image may at large integration angles typically be 7 range samples times 50 azimuth samples, and $\tilde{\boldsymbol{\mu}}_s(\gamma_p, \boldsymbol{\theta})$ is a vector with 350 elements and the size of covariance matrix is therefore $350*350$ elements.

Algorithm 1. The Main Steps in the Procedure to Obtain Estimation Bounds

---

Procedure GenerateEstimationBound
Input : $\boldsymbol{\theta}$, SCR, SNR, γ_p, ϕ
Output : $\sigma_{\hat{\boldsymbol{\theta}}}^2$
Image $= \text{GenerateSARImage}(\gamma_p, \boldsymbol{\theta}, \phi)$
$\tilde{\boldsymbol{\mu}}_s(\gamma_p, \boldsymbol{\theta}, \phi) = \text{GenerateVector}(\text{Image})$
$\mathbf{C}_{\tilde{\mathbf{x}}} = \text{GenerateCovarianceMatrix}(\gamma_p, \phi)$

For $par1 = 1 : \text{Length}(\boldsymbol{\theta})$
For $par2 = 1 : \text{Length}(\boldsymbol{\theta})$

$\quad \mathbf{I}(par1, par2) = 2\text{Re}\left[\dfrac{\delta\tilde{\boldsymbol{\mu}}_s^{\text{H}}}{\delta par1} \mathbf{C}_{\tilde{\mathbf{x}}} \dfrac{\delta\tilde{\boldsymbol{\mu}}_s}{\delta par2} \right]$

end
end

$\mathbf{C}_{\hat{\boldsymbol{\theta}}} \geq \mathbf{I}^{-1}(\boldsymbol{\theta})$
$\sigma_{\hat{\boldsymbol{\theta}}}^2 = \text{diag}\left(\mathbf{I}^{-1}(\boldsymbol{\theta})\right)$

Although the example of the method is selected according to the published results given in [8,13], the example uses a smaller relative bandwidth. In Fig. 3, the relative bandwidth $B_r = 1$ has been used in comparison to $B_r = 1.3$ in [8, 13]. The reason for the lower bandwidth is nonorthogonal sidelobes of the targets [31] causing the dependency between diagonal samples. This effect always appears in the following cases: extremely high relative bandwidth, i.e. UWB, small signal bandwidth in combination with wide integration angle, and vice versa, in large signal bandwidth in combination with a narrow integration angle. Hence, with the selected radar parameters, this effect occurs due to the narrow integration angle and large signal bandwidth, i.e., the resolution is mismatched. In the following calculations we have to set the values of the backscattering strength and the noise level in (15) and (18). The signal-to-noise ratio (SNR) is the relation between the moving target and the noise whereas the signal-to-clutter ratio (SCR) is the relation between moving target and the clutter. Because the SAR process increases the signal relation to the clutter and noise the SCNR and SNR are given at maximum integration angle. This means that the SCR and SNR are smaller at narrower integration angles. In this illustration, we have set SCR to 10 dB and SNR to 20 dB at a maximum integration angle of $32°$. For each clutter scatterer, the SAR process will add the scatterers backscattered signal coherently for each pulse and at the same time the resolution will increase. If the target is a single point-like scatterer and the clutter consists of many scatterers, an increase in resolution will raise the SCR. Since noise is added incoherently between pulses, the SNR increases as the number of pulses increases. Since the processing speed
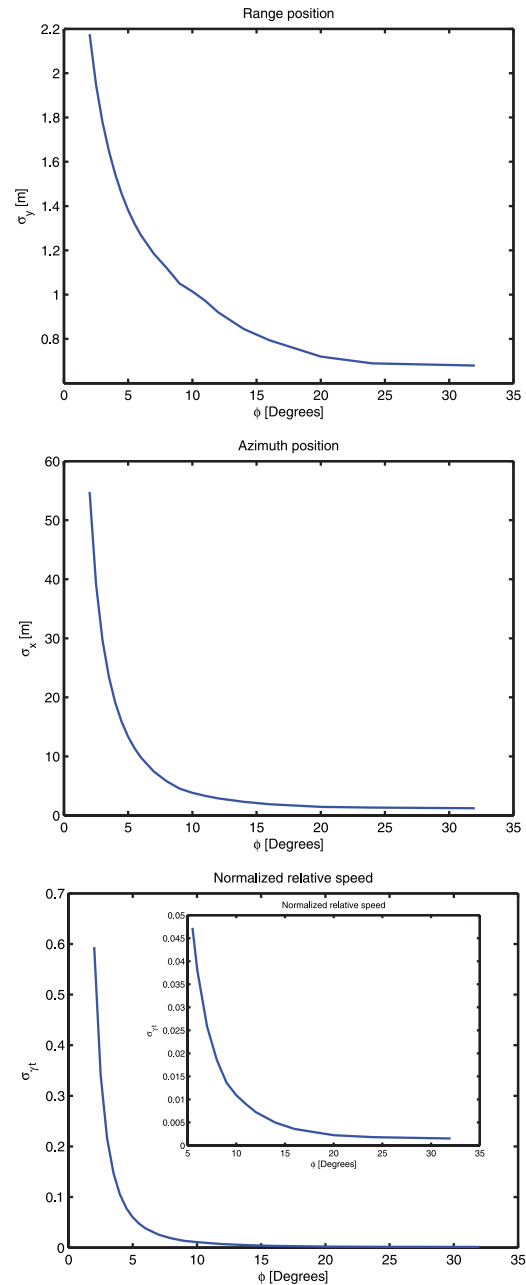

Fig. 3. Lower bounds on standard deviation of estimates for range, azimuth, and NRS calculated using parameters of Table I. Lower bounds are given as function of integration angle.

is $\gamma_p = 1$ to estimate the bound, the moving target is unfocused. However, we use the peak signal power of the focused target, i.e., $\gamma_p = \gamma_T$, to estimate SCR and SNR. This means that the used peak signal power is much higher than that in the bound estimate images when $\gamma_p = 1$. The peak signal power corresponding to $\gamma_p = 1$ is quite low due to the smearing effect. However, the total signal energy of the target should be the same in both cases.

The results from the simulations are shown in Fig. 3. In Fig. 3, the lower bound in range is shown. Even at low integration angles, the target can be measured with high range precision, i.e., $\sigma_{\hat{Y}_0} = 2.5$ m. As the integration angle

increases, the precision increases. At the integration angle of 32°, the lower bound of the standard deviation is down to $\sigma_{\hat{Y}_0} = 0.7$ m. By making a log-log plot of the result, the slope is found to be almost a straight line at low integration angles with an increasing deviation at higher angles. The slope of the curve shows that the lower bound is almost inversely proportional to the square root of the integration angle ($\sigma_{\hat{Y}_0} \propto \phi^{-0.5}$). This relates to the known relation of all pulse radars; standard deviation in range is inversely proportional to the square root of the number of pulses or SNR [36, 37].

In Fig. 3, the lower bound of standard deviation is shown for the azimuth direction. In this case, the resolutions at narrow integration angles are low in comparison with the range resolution. At the narrowest integration angle, the lower bound of the standard deviation is found to be $\sigma_{\hat{X}_0} = 57$ m. However, the slope is very steep in this case. Thus, the lower bound of the standard deviation is down to $\sigma_{\hat{X}_0} = 1.2$ m at the integration angle of 32°. Described in a log-log plot, the slope of this curve is also found to be almost a straight line. Also in this case there is an increasing deviation at the higher integration angles with respect to the straight line. The found slope indicates that the lower bound is also almost inversely proportional to the square root of the cube of the integration angle, ($\sigma_{\hat{X}_0} \propto \phi^{-1.5}$). It is a stronger slope than that in range direction. However, this is reasonable because the resolution increases proportionally to $\phi^{-1.0}$ and the SNR to $\phi^{-0.5}$ at low integration angles. The result is therefore in line with the resolution determined precision given in [21] where the precision is inversely proportionally to integration time, i.e., integration angle.

In Fig. 3, the lower bound of the NRS is presented. At low integration angles, the estimation performance is almost useless. Hence, the value $\sigma_{\hat{\gamma}_t} = 0.61$ is equivalent to 61 m/s in uncertainty of the target's relative speed. However, the slope in this case is much steeper than the others. At 32°, the lower bound of the standard deviation is down to $\sigma_{\hat{\gamma}_t} = 0.0015$ which corresponds to a speed of 0.15 m/s. Using a log-log plot, the slope of this curve is also found to be almost a straight line and with an increasing deviation at the higher integration angles. The slope of the curve shows that the lower bound is approximately inversely proportional to the integration angle with the power factor of 2.5, i.e., $\sigma_{\hat{\gamma}_t} \propto \phi^{-2.5}$. The result is therefore in line with the resolution determined precision given in [21] where the precision is inversely proportionally to the square of the integration time, i.e., integration angle.

Finally, the lower bound was calculated according to the measurements in [8, 13]. The radar parameters used in these measurements are similar to the ones listed in Table I with some discrepancies, however that is mentioned later. The data set are of the real measurements made over open sea, land, and forest. The measurements are performed by the CARABAS II system and they

illustrate two cases of moving targets, one boat at open sea and one simulated target in the forest. In the forest, a target has been simulated in the data according to [13]. The radar parameters are similar to Table I and given by $r_{\min} = 9922m$, $f_c = 52MHz$, $B_r = 1.15$, $\gamma_T = 1.0155$, $\phi = 60°$, $SNR = 15.7dB$ and $SCR = 5.7dB$. This bandwidth and integration angle results in an increase in correlation between image pixels in comparison with simulations presented in Fig. 3. However we still use the independency between pixels as discussed in previous sections. In the calculations, the lower bound of the estimates are found to be $\sigma_{\hat{X}_0} = 1.67m$, $\sigma_{\hat{Y}_0} = 1.00$, and $\sigma_{\hat{\gamma}_t} = 0.0007$ which refers to a standard deviation in speed of 0.09 m/s. In [13], the error between estimated speed and the true speed was found to be 0.07 m/s. Although one sample of the estimator performance does not give any significance to the estimator performance, we can conclude that the estimate error has the same order as the lower bound.

In the second case [8], the moving target is a real ship moving on the sea surface. The radar parameters are $r_{\min} = 7200m$, $f_c = 52MHz$, $B_r = 1.15$, $\phi = 30°$, $SNR = 35.7dB$. At these frequencies, the scattering from the water is very low, actually much below the noise floor, and therefore SNR $\gg$ SCR. The bandwidth is higher than that in Table I but the integration angle is the same. In this case, we do not know the true speed. However, from the broadening of the target given by [8, Fig. 15] and from the SNR, we can at least say that the lower bound is realistic. Performing lower bound estimates are found to be $\sigma_{\hat{X}_0} = 0.064m$, $\sigma_{\hat{Y}_0} = 0.023$, and $\sigma_{\hat{\gamma}_t} = 8.2 \cdot 10^{-5}$ which refers to a standard deviation in speed of 1 cm/s. The error is very small because the SNR is high. With a SNR of 35.7 dB, the noise fluctuation at the peak given by [8, Fig. 15] is very small. Because the noise E_{noise} is related to SNR and the target, we have approximated the fluctuation of the peak to $S_T^2 \pm E_{noise} = S_T^2 (1 \pm 1/SNR)$. In [8, Fig. 15] this would approximately refer to 0dB $\pm 8.2 \cdot 10^{-5}$dB. The broadening at this value is hard to investigate based on [8, Fig. 15]. However, the standard deviation seems to be reasonable because the broadening is almost flat surrounding the peak in the figure. We therefore believe that the derived calculated lower bounds for the real data are a good estimate if compared with the results from the experiments.

X. CONCLUSION

In this paper we propose a method to measure the precision of range and azimuth positions as well as range and azimuth speed estimations performed by a multichannel SAR system. A multichannel UWB SAR can measure two positions as well as two speed components of the moving target. The used method is based on CRLB and the limitations that implies to clutter and noise. The target and the SAR platform are assumed to move with constant speed, i.e., without acceleration. To illustrate the method the precision was determined for a single-channel UWB SAR system. The single channel was chosen because of two different reasons. In a single channel we have found a realistic covariance matrix, a covariance matrix we do not know in the multichannel case. In the single-channel case there are in literature results to compare with; in the multichannel case there are not. In the illustrated example it is found that the estimate of the lower bound variance of range, azimuth, and relative speed changes according to what can be expected in comparison with results in the literature. Finally it is shown that the precision of relative speed can be very high if long integration time is used.

ACKNOWLEDGMENT

REFERENCES

[1] Soumekh, M.
Moving target detection in foliage using along track radar monopulse radar.
IEEE Transactions on Image Processing, **6**, 8 (1997), 1148–1163.

[2] Ender, J. H. G.
Detection and estimation of moving target signals by multi-channel SAR.
International Journal of Electronics and Communications, **50**, 2 (1996), 150–156.

[3] Perry, P. G., DiPietro, R. C., and Fante, R. I.
SAR imaging of moving targets.
IEEE Transactions on Aerospace and Electronics Systems, **35**, 1 (1999), 188–200.

[4] Fienup, J. R.
Detecting moving targets in SAR imagery by focusing.
IEEE Transactions on Aerospace and Electronics Systems, **37**, 3 (2001), 794–809.

[5] Sparr, T.
Moving target motion estimation and focusing in SAR images.
Proceedings of IEEE International Radar Conference, 2005, pp. 290–294.

[6] Gierull, C. G.
Ground moving target parameter estimation for two channel SAR.
IEE Proceedings of Radar Sonar and Navigation, **153**, 3 (2006), 224–233.

[7] Ward, J.
Cramer-Rao bounds for target angle and Doppler estimation with space-time adaptive processing radar.
Conference Record of The Twenty-Ninth Asilomar Conference on Signals, Systems and Computers, 1995, pp. 1198–1202.

[8] Vu, V. T., Sjögren, T. K., Pettersson, M. I., Gustavsson, A., and Ulander, L. M. H.
Detection of moving targets by focusing in UWB SAR – Theory and experimental results.
IEEE Transactions on Geoscience and Remote Sensing, **48**, 10 (2010), 3799–3815.

[9] Ulander, L. M. H., Lundberg, M., Pierson, W., and Gustavsson, A.
Change detection for low-frequency SAR ground surveillance.
IEE Proceedings - Radar, Sonar and Navigation, **152**, 6 (2005), 413–420.

[10] Pettersson, M. I.
Detection of moving target in wideband SAR.
IEEE Transactions on Aerospace and Electronics Systems, **40**, 3 (2004), 780–796.

[11] Cheney, M., and Borden, B.
Theory of waveform-diversity moving-target spotlight synthetic-aperture radar.
SIAM Journal Imaging Sciences, **4**, 4 (2011), 1180–1199.

[12] Jao, J. K., and Yegulalp, A.
Multichannel synthetic aperture radar signatures and imaging of a moving target.
Inverse Problems, **29**, 5 (2013).

[13] Sjögren, T. K., Vu, V. T., Pettersson, M. I., Gustavsson, A., and Ulander, L. M. H.
Moving target speed estimation and refocusing in SAR images.
IEEE Transactions on Aerospace and Electronics Systems, **48**, 3 (2012), 2426–2436.

[14] Dias, J. M. G., and Marques, P. A. C.
Multiple moving target detection and trajectory estimation using a single SAR sensor.
IEEE Transactions on Aerospace and Electronics Systems, **39**, 2 (2003), 604–624.

[15] Zhou, F., Wu, R., Xing, M., and Bao, Z.
Approach for single channel SAR ground moving target imaging and motion parameter estimation.
IET Radar, Sonar & Navigation, **1**, 1 (2007), 59–66.

[16] Kirscht, M.
Detection and imaging of arbitrarily moving targets with single-channel SAR.
Proceedings of IEE Radar Sonar and Navigation, **150**, 1 (2003), 7–11.

[17] Marques, P. A. C., and Dias, J. M. B.
Velocity estimation of fast moving targets using a single SAR sensor.
IEEE Transactions on Aerospace and Electronic Systems, **41**, 1 (2005), 75–89.

[18] Suo, Z., Li, Z., and Bao, Z.
Multi-channel SAR-GMTI method robust to coregistration error of SAR images.
IEEE Transactions on Aerospace and Electronics Systems, **46**, 4 (2010), 2035–2043.

[19] Cerutti-Maori, D., Gierull, C. H., and Ender, J. H. G.
Experimental verification of SAR-GMTI improvement through antenna switching.
IEEE Transactions on Geoscience and Remote Sensing, **48**, 4 (2010), 2066–2075.

[20] Sharma, J. J., Gierull, C. H., and Collins, M. J.
Compensating the effects of target acceleration in dual-channel SAR-GMTI.
IEE Proceedings - Radar, Sonar and Navigation, **153**, 1 (2006), 53–62.

[21] Minardi, M. J., Gorham, L. A., and Zelnio, E. G.
Ground moving target detection and tracking based on generalized SAR processing and change detection.
Proceedings of SPIE, Vol. 5808, *SPIE Conference on Algorithms for Synthetic Aperture Radar Imagery XII*, 2005, pp. 156–165.

[22] Pettersson, M. I.
Optimum relative speed discretization for detection of moving objects in wide band SAR.
IET Radar, Sonar and Navigation, **1**, 3 (2007), 213–220.

[23] Ender, J. H. G., Gierull, C. H., and Cerutti-Maori, D.
Space-based moving target positioning using radar with a switched aperture antenna.
IEEE International Geoscience and Remote Sensing Symposium (IGARSS 2007), 2007.

[24] Budillon, A., Pascazio, V., and Schirinzi, G.
Estimation of radial velocity of moving targets by along-track interferometric SAR systems.
IEEE Geoscience and Remote Sensing Letters, **5**, 3 (2008), 349–353.

[25] Budillon, A., Pascazio, V., and Schirinzi, G.
Amplitude/phase approach for target velocity estimation in AT-InSAR systems.
IEEE Radar Conference (RADAR '08), 2008.

[26] Pettersson, M. I.
Lower bounds of moving target estimation in low frequency UWB SAR.
International Radar Symposium (IRS), Wroclaw, Poland, 2008, pp.151–155.

[27] Pettersson, M. I.
Extraction of moving ground targets by a bistatic ultra-wideband SAR.
IEE Proceedings - Radar, Sonar and Navigation, **148**, 1 (2001), 35–40.

[28] Pettersson, M. I., Zetterberg, V., and Claesson, I.
Detection and imaging of moving targets in wide band SAS using fast time backprojection combined with space time processing.
Proceedings of MTS/IEEE OCEANS, 2005, Washington, D.C., USA, 2005, pp. 2388–2393.

[29] Raney, R. K.
Synthetic aperture imaging radar and moving targets.
IEEE Transactions on Aerospace and Electronic Systems, **AES-7**, 3 (1971), 499–505.

[30] Ulaby, F. T, Moore, R., and Fung, A. K.
Microwave Remote Sensing- Active and Passive,
Vol. 2 - *Radar Remote Sensing and Surface Scattering and Emission Theory.* Reading, MA: Addison-Wesley, 1982.

[31] Vu, V. T., Sjögren, T. K., Pettersson, M. I., and Hellsten, H.
An impulse response function for evaluation of UWB SAR imaging.
IEEE Transactions on Signal Processing, **58**, 7 (2010), 3927–3932.

[32] Chauhan, N. S., Lang, R. H., and Ranson, K.
Radar modeling of a boreal forest.
IEEE Transactions on Geoscience and Remote Sensing, **29**, 4 (1991), 627–638.

[33] Jao, J. K.
Theory of synthetic aperture radar imaging of a moving target.
IEEE Transactions on Geoscience and Remote Sensing, **39**, 9 (2001), 1984–1992.

[34] Kay, S. M.
Fundamentals of Statistical Signal Processing - Estimation Theory. Upper Saddle River, NJ: Prentice-Hall, 1993.

[35] Vu, V. T., Sjögren, T. K., and Pettersson, M. I.
On synthetic aperture radar azimuth and range resolution equations.
IEEE Transactions on Aerospace and Electronic Systems, **48**, 2 (2012), 1764–1769.

[36] Skolnik, M. I.
Radar Handbook. New York: McGraw-Hill, 1970.

[37] Whalen, A. D.
Detection of Signals in Noise. New York: Academic Press, 1971.

Mats I. Pettersson (M'05) received an M.Sc. in engineering physics, a Licentiate degree in radio and space science, and a Ph.D. in signal processing, all from Chalmers University of Technology, Sweden.

He has worked at Ericsson Mobile Communication and for ten years he was employed at Swedish Defence Research Agency (FOI). At FOI, he worked as a research manager and a researcher, mainly focusing on ultrawideband low frequency SAR systems. Since 2005, he has been employed at Blekinge Institute of Technology where he is a professor and research director. His work is related to radar and sonar signal processing where his main interests are SAR inversion and processing, space time adaptive processing (STAP), and sparse passive underwater arrays.

Thomas K. Sjögren (SM'06—M'12) was born in Sundsvall, Sweden, in 1982. He received the M.Sc. degree in space engineering from Luleå University of Technology (LTU), Luleå, Sweden, in 2006 and the Licentiate and Ph.D. degrees in applied signal processing from Blekinge Institute of Technology (BTH), Karlskrona, Sweden, in 2010 and 2012, respectively.

Since 2013, he has been with the Swedish Defence Research Agency (FOI), Linköping, Sweden, focusing on algorithm development for VHF and UHF synthetic aperture radar (SAR). His research interests include moving target detection, parameter estimation, and clutter suppression methods in SAR, particularly wideband SAR and on VHF/UHF band.

Dr. Sjögren is the author and coauthor of about 50 professional publications, including ten IEEE journal articles.

Viet Thuy Vu (S'06—M'12) was born in Hanoi, Vietnam. He received the Diploma degree in electronics at Hanoi University of Technology, Vietnam, the Master of Science degree in communication engineering at the University of Duisburg-Essen, Germany, the Licentiate in applied signal processing at the Blekinge Institute of Technology (BTH), Sweden, and the Doctoral degree in applied signal processing also at BTH in 2011.

He is currently a postdoctoral research associate at BTH. His research interests are mono- and bi-static UWB SAR signal processing, applications of UWB SAR in moving target detection and estimation.

Dr. Vu is the author and co-author of more than 50 professional publications. In 2007, he was awarded the Student Paper Prize at the IET International Conference on Radar Systems.